

# Validation of Interface Capturing and Tracking Techniques with different Surface Tension Treatments against a Taylor Bubble Benchmark Problem

Holger Marschall<sup>a</sup>, Stephan Boden<sup>b</sup>, Christoph Lehrenfeld<sup>c</sup>, Carlos J. Falconi D.<sup>d</sup>, Uwe Hampel<sup>b</sup>, Arnold Reusken<sup>c</sup>, Martin Wörner<sup>d</sup>, Dieter Bothe<sup>a,\*</sup>

<sup>a</sup>Center of Smart Interfaces, Mathematical Modeling and Analysis, Technische Universität Darmstadt

<sup>b</sup>Experimental Thermal Fluid Dynamics, Helmholtz-Zentrum Dresden-Rossendorf

<sup>c</sup>Institut für Geometrie und Praktische Mathematik, RWTH Aachen

<sup>d</sup>Karlsruher Institut für Technologie (KIT), Institut für Katalyseforschung und -Technologie

---

## Abstract

The validation and verification of models and numerical methods for interfacial two-phase flow simulation is still a challenge and standards have not yet been established. Mostly comparing with analytical solutions, many validation studies so far have considered simple or simplified two-phase flow scenarios. One reason for this is the lack of freely accessible and detailed experimental data for validation of interfacial two-phase flow solvers.

The Priority Program SPP 1506 *Transport Processes at Fluidic Interfaces* by the German Research Foundation DFG proposes a benchmark problem for validation of interfacial flow solvers by means of specifically designed experiments for Taylor Bubble Flow. The benchmark experiments aim at providing detailed and local data as a basis for validation. This contribution demonstrates its use by assessing and approving the reliability and accuracy of the flow solvers used by several research groups within the priority program. Special emphasis is set upon different approaches to surface tension calculation both for interface capturing and interface tracking methodologies. Data and material can be freely downloaded from the website of SPP 1506 (<http://www.dfg-spp1506.de/taylor-bubble>).

**Keywords:** validation, surface tension treatment, two-phase flow, Taylor bubble, benchmark problem

---

## 1. Introduction

Taylor bubbles are elongated bubbles which almost completely fill the cross-sectional area of (commonly) straight channels – without wetting its confining walls but being surrounded by a thin liquid film. The flow of multiple subsequent Taylor bubbles in a channel is known as *Taylor flow* (also: bubble train flow), where a *liquid slug* separates two subsequent Taylor bubbles.

Taylor flow in narrow channels is used in many micro-fluidic applications, inter alia, micro-process engineering, catalysis (coated monolith reactors), material synthesis, analysis of biological or chemical probes. Recent reviews of Taylor flow are given in [1, 2].

Main advantages of Taylor flow in milli- or micro-channels are its

- high values of specific exchange area (interfacial

area density per unit volume), and consequently its high heat and mass transfer rates,

- low axial dispersion due to separation of bubbles by liquid slugs,
- high mixing rates within the liquid slugs due to recirculation and
- short diffusion lengths for mass transfer from the gaseous phase through the thin liquid film to the channel wall (e.g., a catalytic wash-coat).

### 1.1. Hydrodynamics of Taylor bubbles

The hydrodynamics of Taylor bubbles in small (milli/micro-) channels is predominately determined by viscous (friction) and surface tension forces, with the inertial forces becoming important only at higher flow velocities. The relevant dimensionless groups are the Capillary number  $Ca = \eta_L U_B / \sigma$  (ratio of viscous to surface tension force) and the Reynolds number  $Re = \rho_L d_h U_B / \eta_L$ , where  $U_B$  denotes the magnitude of the

---

\*Corresponding Author: Dieter Bothe ([bothe@csi.tu-darmstadt.de](mailto:bothe@csi.tu-darmstadt.de))  
Contract/grant Sponsor: German Research Foundation DFG, Priority Program 1506

bubble velocity,  $d_h$  the hydraulic diameter of the channel,  $\sigma$  the surface tension coefficient, and  $\rho_L$  and  $\eta_L$  the liquid density and dynamic viscosity, respectively.

As for the current state of scientific knowledge, it is stated in [1] that, while hydrodynamics of formed Taylor bubbles in fully developed flow and pure liquid systems is generally understood for cylindrical channels, further research is especially required for non-cylindrical channels. Since the interfacial area density is a central measure with respect to process intensification and performance of milli/micro-apparatus, the surface of a Taylor bubble at specific operation conditions is of pivotal interest. Moreover, diffusion lengths in Taylor bubble flow are directly related to process intensification and performance as well. Hence, due to their direct accessibility, relevant target quantities of experimental and theoretical studies are mostly related to the bubble's geometry:

*liquid film thickness.* For cylindrical channels of diameter  $d$  the liquid film thickness  $\delta$  is constant along the circumference of the bubble surface for a wide range of  $Ca$  and can be described by  $\delta/d = 0.66 Ca^{2/3} / (1 + 3.33 Ca^2/3)$  – cf. [3, 4]. The effect of inertial forces on the liquid film thickness is not significant up to  $Re \approx 10$ .

For quadratic channel cross-sections, it is known that the liquid film thickness is not constant, but varies along the circumference of the bubble's surface. For  $Ca$  in the range  $0.04 \dots 0.1$  transition takes place and the Taylor bubble can no longer be considered axis-symmetric [5, 6], while for even lower values of  $Ca$  the bubble clearly penetrates into the corners of the channel.

*bubble shape.* The front and rear end of the bubble obey the shape of hemispheres for low values of  $Ca$ . The higher the values of  $Ca$ , the lower the interfacial curvature on the channel axis at the bubble rear and the higher the curvature at its front. For high values of  $Ca$  the bubble's rear shows a dent, where the curvature of the trailing menisci becomes negative. Within the liquid slug a bypass flow can be observed for  $Ca > 0.7$ , while for  $Ca < 0.7$  there is a recirculation flow.

For quadratic channel cross-sections the shape deformation of the Taylor bubble's front and rear is known to behave qualitatively similar to the circular case. Latest three-dimensional numerical studies [7] of Taylor bubble flow of viscous squalane and nitrogen in a quadratic channel show steepening of the front shape and flattening at the bubble's

rear – in good agreement with experimental results. However, this study has been restricted to moderate/high values of  $Ca$ .

## 1.2. Validation benchmark with Taylor bubbles

Taylor bubbles as a validation benchmark provide the essential advantage of being predominantly governed by the Capillary number as control parameter: for given fluids the Capillary number can be varied by one to two orders of magnitude by changing the bubble velocity. Alternatively, an even larger variation can be achieved by changing the liquid's viscosity. A pivotal measure for validation of the hydrodynamics, employing different numerical methods and codes is the three-dimensional shape of the Taylor bubble for distinct values of  $Ca$ .

In this study, we perform Direct Numerical Simulations (DNS) of a single rising Taylor bubble in a square milli-channel, in order to examine the influence of various numerical methods for surface tension calculation for both interface capturing and interface tracking methods. Hence, our main focus is on the quantitative comparison of the shape of a rising Taylor bubble by means of geometrical target quantities (such as distances, curvatures and film thickness) at locations, where deficiencies in surface tension calculation procedures become visible. We compare different interfacial two-phase solvers and their underlying numerical methods – namely the Volume-of-Fluid (VoF) and Level-Set (LS) interface capturing methods as implemented in the codes FS3D, TURBIT-VOF and DROPS, and the Arbitrary Lagrangian Eulerian (ALE) interface tracking method of OpenFOAM – with detailed and local data obtained by high-resolution X-ray tomography. In doing so, we present a code-to-experiment comparison for a realistic three-dimensional Taylor bubble flow problem, rather than performing a pure (numerical) code-to-code comparison for a two-dimensional benchmark problem (as is mostly done, cf. [8] for instance). Clearly, within the scope of this paper we cannot explain all numerical techniques used in these solvers. Instead, for each of the solvers we outline the main numerical components and give references to relevant literature for further information. Consequently, our focus shall not be on pure numerical target quantities (relative error norms, convergence orders etc.) and computational costs resp. efficiency (computation time). However, since the present flow problem exhibits a low capillary number, and thus the numerical treatment of surface tension is an important issue, we provide a detailed description of the numerical methods used for surface

tension calculation. This also illustrates that very different approaches are used in the four solvers that we validate against the proposed Taylor bubble benchmark.

The remainder of the paper is organized as follows. In the upcoming section we briefly describe the experimental setup as well as data processing enabling us to perform a quantitative comparison with the experimental data obtained from X-ray tomography. Section 3 describes the theoretical basis of the numerical simulations performed. We set out both the underlying mathematical model and the numerical methods of the interfacial two-phase flow solvers employed in this study. Emphasis is put upon the methodology and numerical approximations for surface tension calculation. Next, we present the numerical results along with a discussion on quality and errors (Section 4). Finally, section 5 provides a summary and conclusions.

## 2. Experiment

Experimental investigations aiming at the disclosure of hydrodynamic properties of Taylor bubble flow such as wall film thickness, bubble velocity, slug length and pressure loss were performed by various authors in the past [4, 5, 9–12]. Here, a new measurement principle based on synchrotron X-ray visualization and tomographic reconstruction has been applied to measure the exact shape of rising Taylor bubble in a square millichannel.

### 2.1. Experimental Setup

The experimental setup is schematically depicted in Fig. 1. Within a loop, the liquid is pumped through a vertically aligned square borosilicate glass capillary with a wall thickness of approximately 0.25 mm. The hydraulic diameter was determined to be  $1,979\ \mu\text{m}$ . Pressurized air was injected into the liquid by means of a high-speed injection valve. The valve was attached to the remaining port of the T-junction at the lower end of the capillary tube. The length of the capillary was  $90\ d_h$ . The consumed two-phase mixture was fed through a flexible tube at the top of the capillary back to the liquid container, where the gas is separated from the liquid. By controlling pump power and inlet tube resistance the fluid velocity was varied. Then, by changing the duty cycle of the valve, the specific Taylor bubble flow regime was produced. The temperatures of the fluid were measured both at the entrance and at the exit of the capillary.

The visualization experiments were conducted at the synchrotron radiation source ANKA (Karlsruhe Institute of Technology). White X-ray radiation provided at

the TOPO/TOMO beamline [13] was used to project a  $1.78\ \text{mm}$  by  $2.31\ \text{mm}$  wide portion of the capillary at a distance of  $70d_h$  above the gas injection valve onto a fast X-ray image detector. The detectors high-speed camera was read out at frame rates up to 36,000 fps. Beside producing plain radiographic images, the capillary was also very slowly rotated during the passage of a bubble train by means of a linear rotary motor within a limited range of angular positions. In doing so, a set of tomographic projection images has been produced showing the bubbles at different projection angles, which is required for the reconstruction of the three-dimensional bubble shape.

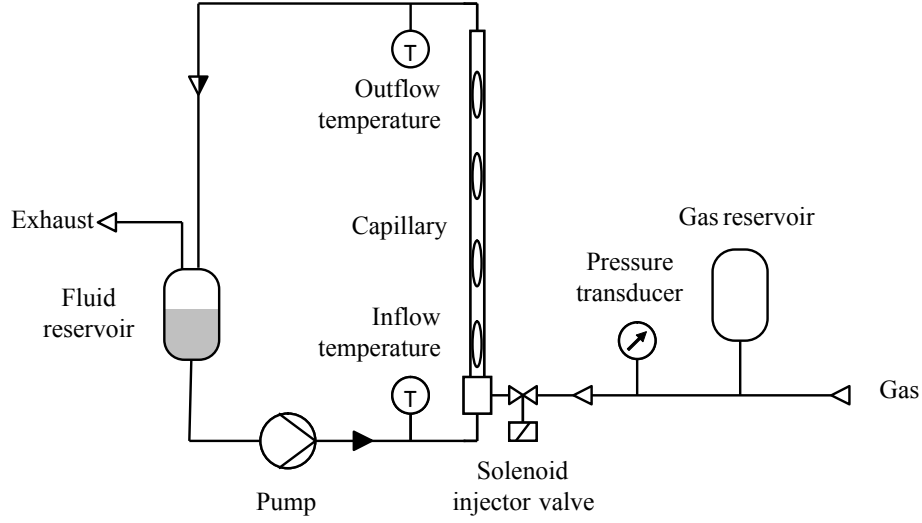
### 2.2. Data processing

Image processing algorithms were used to extract the bubble shape information from the images. Since the recorded images only show a part of the bubble due to the restricted field of view, a visualization of the whole bubble was created by superposition of consecutive raw X-ray images. The bubble's instantaneous velocity was measured by following its tip positions as the bubble moves through the field of view. The bubble's length was calculated from the previously determined instantaneous velocity and the time duration that elapsed between the occurrences of the front and rear meniscus crossing the center of the image. A careful analysis of the image brightness distribution at the edge of the projected bubble was performed and thus the projected liquid film thickness – i.e. the distance between the bubble's interface and the channel's edge – was obtained. The well known backprojection reconstruction algorithm was used to obtain the three-dimensional shape from the projection images. Since the bubbles' tips served as reference points for image registration, the reconstruction was only possible for the bubble front and rear shape. From these results, both the lateral and diagonal film thickness was obtained.

### 2.3. Experimental Results

An aqueous solution of 76.9% glycerol (Sigma Aldrich 49770) and 23.1% deionized water was used as liquid. The difference between the inlet- and outlet temperature of the liquid was 2.7 K, and the average temperature at the position where the X-ray beam impinges the capillary was estimated to be  $27.9^\circ\text{C}$ . Using tabulated values for density, surface tension and viscosity [14], the Capillary and Reynolds number were determined to be  $\text{Ca} = 0.088$  and  $\text{Re} = 17.0$ .

Since the total capture time of the high speed camera was limited to 4.7 s for the chosen frame rate of



**Figure 1:** Sketch of the experimental setup.

36,000 fps, only three bubbles were captured during the experimental run, of which only one bubble is considered here. Also, the imaging window height was substantial shorter than the observed bubble. Fig. 2a shows a superimposed image of the Taylor bubble as a result from all X-ray images of that single bubble superimposed at their calculated positions and after subtracting the structures of the glass capillary from the picture. The bubble velocity was measured to be 205.6 mm/s at the moment as it passed the X-ray beam; the length of the bubble was 7.2 mm. Fig. 2b shows the bubble's contour as it was determined from Fig. 2a – with sub-pixel resolution at the edge of the bubble where the image brightness crosses the background intensity level.

The tomographic dataset consisted only of 351 projections, which thus resulted in a rather noisy reconstruction. Moreover, the tomographic dataset covered only an angular range of  $128^\circ$ , therefore only roughly a quarter of the reconstruction was considered to be valid. The reconstructed data was scanned at different heights and the axial and diagonal bubble shape was fitted using polynomial splines. The so determined axial bubble shape was then scaled to bring it in coincidence with the axial bubble shape from the two-dimensional projection. Fig. 3 shows both axial and diagonal bubble shape for comparison. Splines were used to estimate the bubbles cross section using the information from axial and diagonal radii. From this, the bubble volume was calculated to be  $17.5 \text{ mm}^3$ .

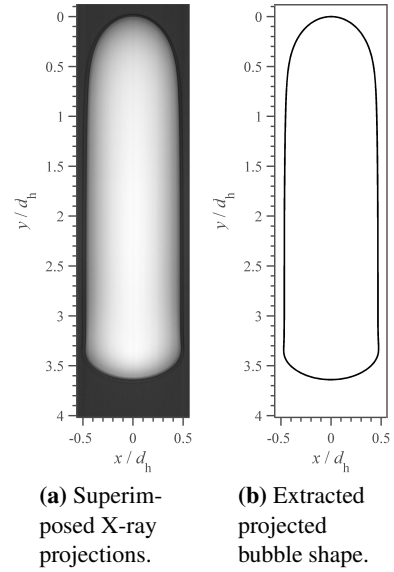


**Figure 2:** Superimposed X-ray projections of a single Taylor bubble moving in a square capillary. The walls of the capillary are removed from the image by subtraction (left). The extracted projected axial bubble shape (right).

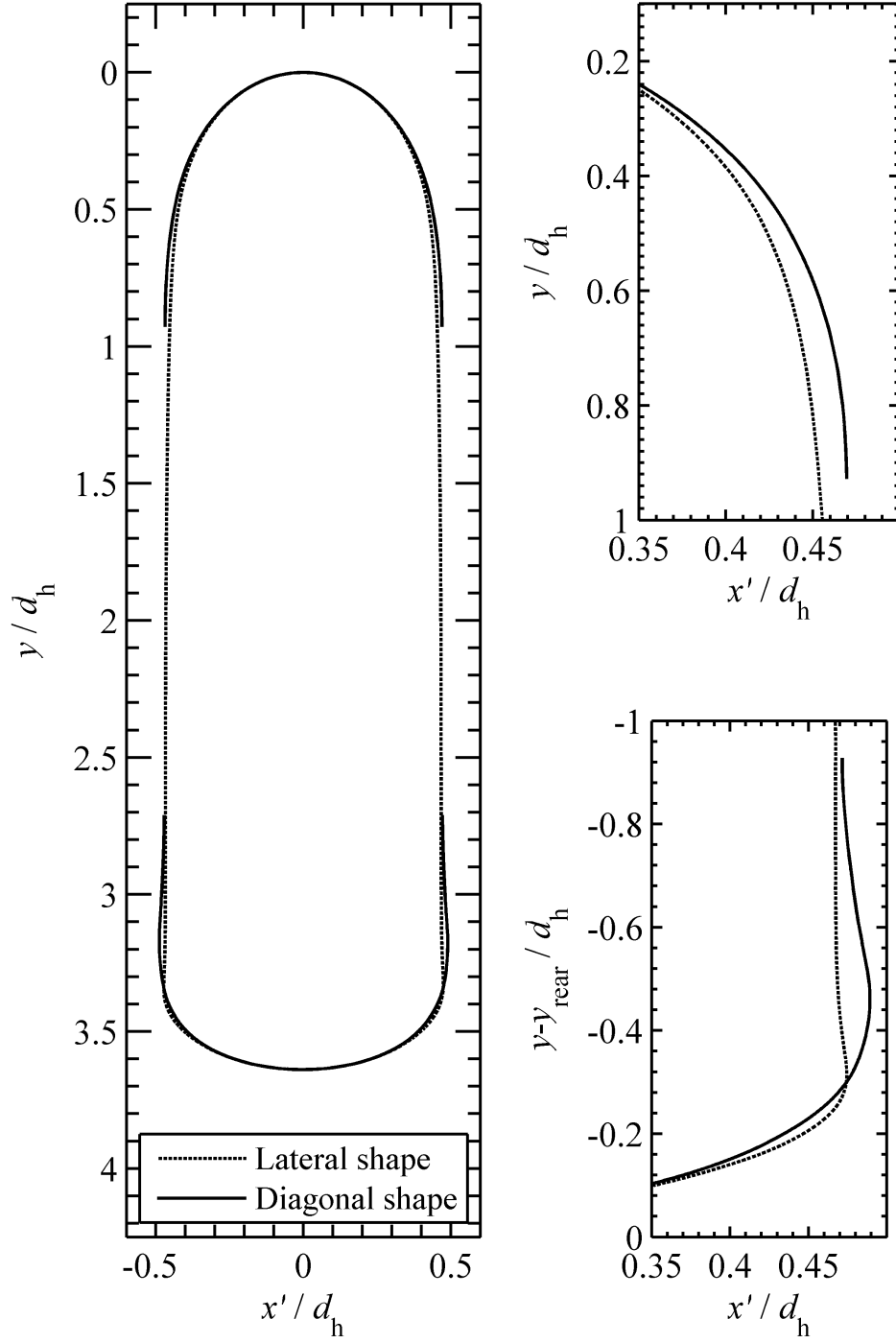


**Figure 3:** Axial and diagonal bubbles shapes.

Data from other experimental runs confirmed, that the bubble velocity fluctuated by 0.7%, and the bubble length fluctuated by 1.5%, each from bubble to bubble. However, the obtained plots of the projected bubble interface at the front and the rear did not vary between each other in the direction normal to the interface by more than 0.1% with respect to the hydraulic diameter. The uncertainty of the bubble's volume  $V$  might be approximated if we consider a cylindrical bullet of length  $l$  and radius  $r$ . The relative error is then  $\Delta V/V = \Delta l/l + 2\Delta r/r$ . The bubble length was computed from the bubble velocity, which itself was determined by detecting the passage of the bubble's tip and rear in the images at a precision of 0.39% resulting from the uncertainty of the linear regression of the tracked tip positions over a distance of about 204 pixel within 200 consecutive frames each. As the uncertainty in the extracted bubble shape is 0.1%, the radii thus were extracted at a precision of  $2\mu\text{m}$ . Thus  $\Delta V/V$  is at least 0.41% for the above described bubble. Moreover, the accuracies of calculated capillary and Reynolds number are dictated mostly by the variance of liquid's viscosity, which is a function of the liquids temperature. Temperature measurements of the liquid at the inlet and the outlet of the capillary were done at a precision of  $\pm 0.5\text{ K}$ , with in turn causes the uncertainties of  $\text{Ca}$  and  $\text{Re}$  to be 3.5%. Additional 0.5% uncertainty in these values resulted from the limited detector resolution of  $5\mu\text{m}$ . The radiographic projections show (due to the highly redundant data) superior image quality and are thus privileged to serve as reference for bubble shape measurements. The tomographic reconstruction however still suffered from the high noise level and thus still required the application of spline interpolation to obtain three dimensional shapes. Furthermore, the projection data was gathered from a set of consecutive bubbles, thus the 3D reconstruction corresponds only to the ensemble average of the bubble train. Despite their slight inaccuracies we consider the experimental results to be of interest, since for the first time a three dimensional measurement of the bubble's shape has been accomplished.

### 3. Numerical Simulations

In order to perform direct numerical simulations (DNS) of two-phase interfacial flows, in principal two methodologies are to be distinguished, namely interface capturing and interface tracking. While the first family of methods *captures* the position of a fluid interface from a marker field stored on a spatially fixed computational mesh, the latter family directly *tracks* the in-

terface position by utilizing a moving mesh approach, in which the interface itself is aligned to a set of cell faces, or by employing a surface mesh moving relative to a fixed volume mesh. The latter approach, so-called Front tracking [15], is not considered below, since it has not been applied in this work.

This study is concerned with both the interface capturing (ICM) and the interface tracking methodology (ITM): as for the ICM we consider a Level-Set method [16–19] and two Volume-of-Fluid methods [20–22]; as for an ITM we consider the Arbitrary Lagrangian Eulerian method [23, 24]. The methods are implemented in the Finite Element code DROPS and the Finite Volume codes FS3D, TURBIT-VOF and OpenFOAM (interTrackFoam)<sup>1</sup>, respectively. Both methodologies are based on the two-phase Navier-Stokes equations presuming a sharp jump of continuum mechanic properties at the interface (sharp interface model). The fluid interface itself is a surface of discontinuity of zero thickness, which separates both fluid phase regions, for which we consider two incompressible, Newtonian, immiscible and isothermal fluids.

#### 3.1. Mathematical Model

Employing the surface Reynolds transport and divergence theorem, the integral balance of a general intensive quantity  $\psi$  reads

$$\begin{aligned} & \int_{V \setminus \Sigma(t)} (\partial_t \psi + \nabla \cdot (\psi \mathbf{v})) dV \\ & + \int_{\Sigma(t) \cap V} [\mathbf{j} + \psi (\mathbf{v} - \mathbf{v}_\Sigma)] \cdot \mathbf{n}_\Sigma dS \\ & = \int_{V \setminus \Sigma(t)} (-\nabla \cdot \mathbf{j} + f) dV + \int_{\Sigma(t) \cap V} (-\nabla_\Sigma \cdot \mathbf{j}_\Sigma + f_\Sigma) dS, \quad (1) \end{aligned}$$

where  $\mathbf{v}$  denotes the bulk velocity and  $\mathbf{v}_\Sigma$  the interface velocity with  $\Sigma(t)$  representing the fluid interface cutting through an arbitrary fixed control volume  $V \in \Omega$  with  $\Omega = \Omega_1(t) \cup \Omega_2(t)$ .  $\mathbf{n}_\Sigma$  represents the interface unit normal,  $\mathbf{v}_\Sigma$  its velocity.  $f$  and  $f_\Sigma$  denote volume- and area-specific source terms and  $\mathbf{j}$  resp.  $\mathbf{j}_\Sigma$  volume- and area-specific fluxes.

Localization yields the so-called general transport equation for  $\psi$ , i.e.

$$\partial_t \psi + \nabla \cdot (\psi \mathbf{v} + \mathbf{j}) = f \quad \text{in } \Omega_1(t) \cup \Omega_2(t), \quad (2)$$

<sup>1</sup>OpenFOAM comprises of over 80 solvers to simulate specific problems in CCM and over 170 utilities. Hence, in order to avoid ambiguity, a closer specification of at least the used solver family is necessary, which we provide in the brackets.

along with the interfacial jump conditions

$$\llbracket \psi (\mathbf{v} - \mathbf{v}_\Sigma) + \mathbf{j} \rrbracket \cdot \mathbf{n}_\Sigma = -\nabla_\Sigma \cdot \mathbf{j}_\Sigma + f_\Sigma \quad \text{on } \Sigma(t). \quad (3)$$

For incompressible fluids, the transport equations and interfacial jump conditions for mass ( $\psi = \rho$ ) and linear momentum ( $\psi = \rho \mathbf{v}$ ) read

$$\nabla \cdot \mathbf{v} = 0 \quad \text{in } \Omega \setminus \Sigma(t), \quad (4)$$

$$\partial_t(\rho \mathbf{v}) + \nabla \cdot (\rho \mathbf{v} \mathbf{v}) = -\nabla p + \nabla \cdot \boldsymbol{\tau} + \rho \mathbf{g} \quad \text{in } \Omega \setminus \Sigma(t). \quad (5)$$

Herein, the viscous stress tensor for a Newtonian fluid reads  $\boldsymbol{\tau} = \eta(\nabla \mathbf{v} + (\nabla \mathbf{v})^\top)$ .  $\eta$  denotes the dynamic fluid viscosity,  $\rho$  its density, and  $\mathbf{g}$  is the gravitational acceleration. Moreover, the jump conditions at the interface in the common jump notation<sup>2</sup> read

$$\llbracket \mathbf{v} \rrbracket = \mathbf{0} \quad \text{on } \Sigma(t), \quad (6)$$

$$\llbracket p \mathbf{I} - \boldsymbol{\tau} \rrbracket \cdot \mathbf{n}_\Sigma = \sigma \kappa \mathbf{n}_\Sigma \quad \text{on } \Sigma(t), \quad (7)$$

where a constant surface tension coefficient  $\sigma$  (i.e., disregarding Marangoni effects), no phase change (due to evaporation or condensation) and no-slip at the interface has been assumed. Herein,  $\kappa$  denotes twice the mean interface curvature,  $\kappa = \nabla_\Sigma \cdot (-\mathbf{n}_\Sigma)$ .

**Interface Capturing Methodology.** In interface capturing methods, equations (4) and (5) are solved in the so-called *one-field formulation* – inherently taking into account corresponding jump conditions according to (6) and (7). For this one-field formulation specific marker functions are utilized enabling us to capture the interface position implicitly. Then, both density and viscosity fields can be evaluated locally. In Volume-of-Fluid methods this is accomplished by means of a phase indicator function, whereas in Level-Set methods a level-set function is used.

The one-field formulation of the momentum transport according to (5) reads:

$$\begin{aligned} \partial_t(\rho \mathbf{v}) + \nabla \cdot (\rho \mathbf{v} \mathbf{v}) \\ = -\nabla p + \nabla \cdot \boldsymbol{\tau} + \rho \mathbf{g} + \sigma \kappa \mathbf{n}_\Sigma \delta_\Sigma, \end{aligned} \quad (8)$$

where the singular surface tension force has been modified consistently towards a interfacial force density  $\mathbf{f}_\Sigma = \sigma \kappa \mathbf{n}_\Sigma \delta_\Sigma$  due to surface tension. Effectively, the interfacial momentum jump condition is incorporated employing the Dirac distribution  $\delta_\Sigma$ , which is evaluated method-specifically using the corresponding marker function. Details with special emphasis on surface tension treatment are provided in the remainder on a per-method basis.

<sup>2</sup>with jump brackets being defined as  $\llbracket \psi \rrbracket(t, \mathbf{x}) := \lim_{h \rightarrow 0+} (\psi(t, \mathbf{x} + h \mathbf{n}_\Sigma) - \psi(t, \mathbf{x} - h \mathbf{n}_\Sigma))$  for  $\mathbf{x} \in \Sigma(t)$ .

**Interface Tracking Methodology.** In interface tracking methods, the fluid interface itself is represented by a computational mesh boundary. Consequently, interface tracking inherently exhibits an explicit rather than an implicit interface representation of interface capturing methods. The flow of each fluid phase is governed by a separate set of conservation equations in *Arbitrary Lagrangian Eulerian (ALE)* formulation [23, 24] being associated with separate fluid domains and coupled via interfacial boundary conditions. In doing so, interface tracking methods do not impose the interfacial jump conditions according to (6) and (7) within a corresponding one-field formulation of the transport equations, but they enforce them as boundary conditions (incl. the effect of surface tension).

The integral form of the governing equations (cp. (4) and (5) without interfacial terms for a moving (non-material) control volume) reads

$$\frac{d}{dt} \int_{V(t)} dV - \int_{S(t)} \mathbf{v}_S \cdot \mathbf{n} dS = 0, \quad (9)$$

$$\frac{d}{dt} \int_{V(t)} \rho dV + \int_{S(t)} \rho (\mathbf{v} - \mathbf{v}_S) \cdot \mathbf{n} dS = 0 \quad (10)$$

and

$$\begin{aligned} \frac{d}{dt} \int_{V(t)} \rho \mathbf{v} dV + \int_{S(t)} \rho (\mathbf{v} - \mathbf{v}_S) \mathbf{v} \cdot \mathbf{n} dS \\ = \int_{S(t)} \boldsymbol{\sigma} \cdot \mathbf{n} dS + \int_{V(t)} \rho \mathbf{g} dV. \end{aligned} \quad (11)$$

The above equations govern (as before) isothermal flow of incompressible fluid within an arbitrary volume  $V(t)$  bounded by its surface  $S(t)$  with unit normal  $\mathbf{n}$  – namely the so-called Space Conservation Law (SCL) according to (9), mass conservation (10) and linear momentum conservation (11). Herein,  $\mathbf{v}_S$  represents the velocity of  $S$ . For Newtonian fluids, the total momentum flux tensor  $\boldsymbol{\sigma}$  can be decomposed as  $\boldsymbol{\sigma} = -p \mathbf{I} + \boldsymbol{\tau}$  with the viscous stress tensor being modeled for Newtonian fluids as before:  $\boldsymbol{\tau} = \eta(\nabla \mathbf{v} + (\nabla \mathbf{v})^\top)$ .

Note in passing that – as the transport equations for the phase indicator or the level-set is central to the aforementioned interface capturing methods – the SCL according to (9) is central to the interface tracking method. It provides the relationship between the rate of change of the volume  $V(t)$  and the corresponding surface velocity  $\mathbf{v}_S$  causing this change.

### 3.2. Numerical Methods

#### 3.2.1. Level-Set Method

##### – DROPS

As for an *interface capturing method*, we consider the Level-Set method as implemented in the in-house three-dimensional finite element package DROPS [25]. The code is written in C++. It is based on a level-set formulation including non-standard techniques such as an extended finite element method for the pressure approximation and a modified Laplace-Beltrami technique for surface tension computation. For a detailed description the interested reader is referred to [26, 27] and the DROPS internet homepage [28].

**Applied models and methods.** For capturing the a priori unknown interface the level-set method is employed. The level-set function, denoted by  $\phi = \phi(x, t)$ , is a scalar function with  $\phi(x, t) < 0$  for  $x \in \Omega_1(t)$ ,  $\phi(x, t) > 0$  for  $x \in \Omega_2(t)$  and  $\phi(x, t) = 0$  for  $x \in \Sigma(t)$ . Ideally, the level set function is a signed distance function. In this setting, the interface  $\Sigma(t)$  is given only implicitly as the zero-level of the level-set function. The interface motion is described by the linear hyperbolic level-set equation

$$\partial_t \phi + \mathbf{v} \cdot \nabla \phi = 0 \quad (12)$$

for  $t \geq 0$  and  $x \in \Omega$ . With this, the density  $\rho$  and viscosity  $\eta$  can be expressed as jumping coefficients in terms of the level-set function –  $\rho(\phi)$ ,  $\eta(\phi)$ . The effect of the surface tension is expressed in terms of a force localized at the interface. The localized surface tension force is given as  $f_\Sigma = \sigma \kappa \delta_\Sigma \mathbf{n}_\Sigma$  with  $\delta_\Sigma$  the Dirac  $\delta$ -function with support only on  $\Sigma$ . The resulting continuous model (4), (8) and (12) is also used in [29–32], for example.

Solving for equation (12) only in order to capture the interface is insufficient as the level-set function would degenerate over time affecting the treatment of discontinuities and the surface tension. To avoid this a reparametrization scheme for the level-set function was implemented such that  $\phi$  remains close to a signed distance function. Moreover, the reparametrization smoothens the level-set function in the vicinity of the interface and thus stabilizes its evolution. A known problem of the level-set formulation is that mass conservation is not inherently preserved in a discretized formulation. This numerical error in volume, however, vanishes for grid size going to zero. An interface shift is applied to compensate for the volume loss – cf. [26].

**Finite element discretization.** The spatial discretization is based on a multilevel hierarchy of tetrahe-

dral grids. A stable adaptive refinement algorithm [33] has been implemented which allows for higher resolutions close to the bubble surface. As time evolves the grid is updated by refinement and coarsening to keep the higher resolution in the vicinity of the bubble surface.

For the discretization of the flow variables and the level-set function a finite element approach is used – cf. [27]. For the spatial discretization of the velocity  $\mathbf{v}$  and the pressure  $p$  the LBB-stable Hood-Taylor  $P_2$ - $P_1$  finite element pair is used. The pressure space is enriched with a so-called extended finite element method (XFEM) leading to ansatz functions which allow for discontinuities at the approximate zero-level of the level-set functions – cf. [34]. The level-set function  $\phi$  is discretized by continuous piecewise quadratic finite elements. The finite element method for the level-set advection equation (12) is stabilized by a standard streamline diffusion technique [35].

For the finite element discretization of the Navier-Stokes equations, integrals over tetrahedra  $T$  have to be evaluated, having discontinuous integrands (due to discontinuous  $\rho$ ,  $\eta$ ) if  $T$  is cut by  $\Sigma$ . Note that in such cases we do *not* apply any smoothing (e.g., by using a smoothed Heaviside function), but integrate over the parts  $\Omega_i \cap T$ ,  $i = 1, 2$ , where the integrands are continuous and thus standard quadrature rules can be applied. Thus, our approach is a *sharp interface method*. Therefore one needs an approximation  $\Sigma_h$  of the zero level of  $\phi$ . This is done by replacing the piecewise quadratic approximation  $\phi_h$  by a piecewise linear approximation  $\tilde{\phi}_h$  on a once refined mesh. The resulting approximate interface (which is the zero level of  $\tilde{\phi}_h$ ) is piecewise planar which facilitates quadrature significantly. A sketch of the discrete interface resulting from this approach is displayed in Figure 4.

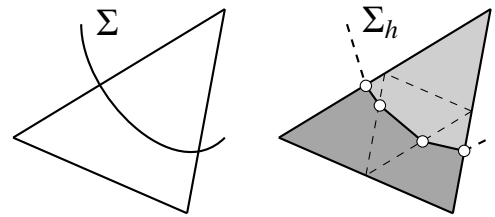


**Figure 4:** Sketch of piecewise linear approximation of interface based on  $\tilde{\phi}_h$  for 2D case.

**Surface tension calculation.** For the numerical treatment of the surface force term  $f_\Sigma$ , a modified Laplace-Beltrami technique is applied to avoid an explicit computation of the curvature which would involve the approximate evaluation of second order derivatives.



As the force is only localized at the interface  $\Sigma$ , its weak formulation is evaluated as a surface integral on  $\Sigma$ .

The surface tension functional

$$f_\Sigma(\mathbf{w}) = -\sigma \int_\Sigma \kappa \mathbf{w} \cdot \mathbf{n} ds$$

is reformulated using the identity  $-\Delta_\Sigma \text{id}_\Sigma = \kappa \mathbf{n}$  and applying partial integration

$$f_\Sigma(\mathbf{w}) = \sigma \int_\Sigma \nabla_\Sigma \text{id}_\Sigma \cdot \nabla_\Sigma \mathbf{w} ds.$$

In order to render the surface tension functional computational feasible, we replace  $\Sigma$  by the approximate interface  $\Sigma_h$ . Thus, integration takes place on the discrete, piecewise planar interface  $\Sigma_h$  constructed from the piecewise linear approximation  $\tilde{\phi}_h$ . The surface gradients  $\nabla_\Sigma$  can be written as  $\mathbf{P}\nabla$ , with the tangential projection  $\mathbf{P} := \mathbf{I} - \mathbf{n}\mathbf{n}^\top$ . In the discretization the choice for an approximate normal  $\mathbf{n}_h$  is crucial. It turns out that using the normal  $\tilde{\mathbf{n}}_h$  to the piecewise planar approximate interface  $\Sigma_h$  leads to a poor approximation. In [34] it was shown for the surface tension functional for the corresponding numerical approximation  $\tilde{f}_{\Sigma_h}$  of the surface tension function  $f_\Sigma$  the error bound

$$\sup_{\mathbf{w} \in \mathbf{W}_h} \frac{f_\Sigma(\mathbf{w}_h) - \tilde{f}_{\Sigma_h}(\mathbf{w}_h)}{\|\mathbf{w}_h\|_1} \leq \sigma c \sqrt{h} \quad (13)$$

holds with a constant  $c$ , the characteristic mesh size  $h$  and the finite element space of continuous piecewise quadratics  $\mathbf{W}_h$ . Numerical examples indicate that this estimate is sharp w.r.t.  $h$ . In [34] it is suggested to use the piecewise quadratic information of  $\phi_h$  to get a more accurate normal  $\mathbf{n}_h = \nabla \phi_h / \|\nabla \phi_h\|$  which is no longer piecewise constant on the discrete interface  $\Sigma_h$ . Putting these ideas together one obtains the discrete surface tension functional as

$$f_{\Sigma_h}(\mathbf{w}) = \sigma \int_{\Sigma_h} (\mathbf{I} - \mathbf{n}_h \mathbf{n}_h^\top) \nabla \text{id}_\Sigma \cdot \nabla_{\Sigma_h} \mathbf{w} ds$$

where  $\nabla_{\Sigma_h}$  denotes the surface gradient w.r.t. the normal  $\tilde{\mathbf{n}}_h$ . Using this discretization of the surface tension functional improves the estimate in (13) resulting in

$$\sup_{\mathbf{w} \in \mathbf{W}_h} \frac{f_\Sigma(\mathbf{w}_h) - f_{\Sigma_h}(\mathbf{w}_h)}{\|\mathbf{w}_h\|_1} \leq \sigma c h. \quad (14)$$

More details concerning the interface approximation and discretization of the surface-tension force term can be found in [27, 34].

### 3.2.2. Volume-of-Fluid Method – FS3D & TURBIT-VOF

As for a second *interface capturing method*, we consider the Volume-of-Fluid methods as they are implemented in the in-house codes FS3D and TURBIT-VOF. Free Surface 3D (FS3D) – cf. [36] – refers to two-phase flows of incompressible Newtonian fluids with significant density and viscosity ratios, which FS3D is able to capture in an accurate, robust and stable manner. The code is written in Fortran being actively developed at ITLR (Univ. Stuttgart) and MMA (Center of Smart Interfaces, TU Darmstadt). The code has been extensively validated, in particular, for hydrodynamics and mass transfer of single rising bubbles with and without reaction [37, 38], Newtonian and non-Newtonian droplet collision [39, 40] and for hydrodynamics of falling films [41], in the course of which its discretization practice and numerical methodology has proven accurate and reliable. The code TURBIT-VOF – cf. [42, 43] – is written in Fortran and has been developed at Karlsruhe Institute of Technology (KIT). TURBIT-VOF solves the two-phase Navier-Stokes equation in non-dimensional single field formulation for two incompressible Newtonian fluids.

**Applied models and methods.** In VOF methods the interface position is captured implicitly introducing the phase indicator  $f_1$  (for brevity  $f$  in the remainder) for one of the phases (e.g. phase 1) along with its corresponding transport equation,

$$\partial_t f + \mathbf{v} \cdot \nabla f = 0, \quad (15)$$

where

$$f(t, \mathbf{x}) := \begin{cases} 1 & \text{if } \mathbf{x} \in \Omega_1(t), \\ 0 & \text{otherwise.} \end{cases} \quad (16)$$

Equation (15) is complemented by (4) and (8) – which comprises the two-phase problem, along with suitable initial and boundary conditions. Herein, the interfacial momentum jump condition according to (7) is incorporated employing the Dirac distribution  $\delta_\Sigma = \|\nabla f\|$ . Note in passing that, while the level-set counterpart  $\|\nabla \phi_h\|$  can be seen in the common manner, the term  $\|\nabla f\|$  is to be understood in the sense of functions of bounded variation [44]. The interface curvature is evaluated as  $\kappa = -\nabla_\Sigma \cdot \mathbf{n}_\Sigma$ , where it is common practice to arrive at an improved numerical approximation of  $\mathbf{n}_\Sigma$  by smoothing the  $f$ -field by means of regularization techniques (mollification).

### FS3D

**Finite Volume discretization.** The Volume-of-Fluid Code FS3D [36] is based on Finite Volume discretization and solves for the two-phase Navier-Stokes equations (4) and (8) along with the phase fraction advection equation (15). The interface is kept sharp during simulations by geometrically reconstructing and advecting the interface, adopting the Piecewise Linear Interface Calculation (PLIC) method [45] and a split advection algorithm [36]. The underlying structured Cartesian grid supports staggered variable arrangement with the velocity field being stored on cell faces and the pressure field correspondingly on cell centers. The code is massively parallelized using MPI and OpenMP.

Time discretization is done using the Euler explicit method. The solution of the pressure Poisson equation is accomplished by a projection method, the matrix being inverted by a geometric multigrid method. The velocity update at each time step is accomplished by means of a projection method [46], the result of which is the Poisson equation for pressure-velocity coupling:

$$\nabla \cdot \left[ \frac{1}{\rho^{n+1}} \nabla p^{n+1} \right] = \frac{\nabla \cdot \tilde{\mathbf{v}}}{\Delta t}, \quad (17)$$

where  $\tilde{\mathbf{v}}$  denotes a temporary velocity field, which has been calculated from the velocity field  $\mathbf{v}^n$  at the old time level, taking into account accelerations (inter alia) due to viscous, momentum and surface tension forces, but excluding the pressure force. The enforcement of a divergence-free (solenoidal) velocity field  $\mathbf{v}^{n+1}$  at the new time level is accomplished by combining the pressure  $p^{n+1}$  from the Poisson equation and the temporary velocity field  $\tilde{\mathbf{v}}$  according to

$$\mathbf{v}^{n+1} = \tilde{\mathbf{v}} - \frac{\Delta t}{\rho^{n+1}} \nabla p^{n+1}. \quad (18)$$

For momentum convection according to (8) Gudonov-Splitting is employed.

**Surface tension calculation.** As indicated before, the momentum jump conditions according to (7) are incorporated by an additional force density  $\mathbf{f}_\Sigma$  taking into account the effect of surface tension. For surface tension modeling, FS3D provides either the Continuous Surface Stress (CSS) [47], Continuous Surface Force (CSF) [48] or balanced CSF (bCFS) [49] method, respectively. Being the most enhanced method with respect to accuracy and stability (cf. parasitic/spurious currents), we employ FS3D along with the balanced Continuous Surface Force in this study, the basics of which shall be briefly described in the remainder of this section.

The basic idea of a balanced-force discretization of  $\mathbf{f}_\Sigma$  is two-fold [49] and related to a careful discretization of

- i) the interfacial curvature  $\kappa$  and
- ii) the volume fraction gradient  $\nabla f$ .

All terms constituting  $\mathbf{f}_\Sigma$  are to be discretized on the face centers of a computational cell rather than its center. Moreover, this has to be accomplished such that its discretized form *exactly balances* with the discretized pressure force. I.e., the discretization has to be done in exactly the same manner that is using the *same computational stencil*.

- ad i) As for an exact evaluation of the interfacial curvature in the context of a balanced-force approach, different methods being based on fitting of paraboloids and/or (generalized) height functions render suitable [49–51]. In this study, we employ FS3D’s implementation of generalized height functions for curvature estimation, following Popinet et al. [51]. The overall algorithm is described best in two parts: the first one comprises of a variable cell stencil algorithm being used for determination of ‘local’ heights relative to a common height level to calculate the interfacial curvature from. In case the mesh resolution becomes insufficient (e.g., in case of highly curved interface topologies), this generalized height function algorithm is accompanied by a local paraboloid fitting algorithm: fitting of a paraboloid to known surface points, stemming from the barycenters beyond reconstructed surfaces (PLIC), is accomplished by means of a least-square fit. Then the curvature can be calculated algebraically. However, this only becomes necessary if the first algorithm part – starting in the direction of the volume fraction gradient – fails to find *any* height function for curvature calculation. Otherwise, for a two-dimensional scenario the curvature in cell  $(i, j)$  from the generalized height function  $h$  in  $x$ -direction is calculated as

$$\kappa_{(i,j)} = \frac{h_{yy,(i,j)}}{(1+h_{y,(i,j)}^2)^{3/2}}. \quad (19)$$

- ad ii) The discretized Poisson equation in  $x$ -direction for cell  $(i, j)$  reads

$$\begin{aligned} \frac{1}{\Delta x} & \left( \frac{p_{(i+1,j)} - p_{(i,j)}}{\rho_{(i+1/2,j)}} - \frac{p_{(i,j)} - p_{(i-1,j)}}{\rho_{(i-1/2,j)}} \right) \\ &= \frac{\tilde{v}_{(i+1/2,j)} - \tilde{v}_{(i-1/2,j)}}{\Delta t}. \end{aligned} \quad (20)$$

Consequently, it is advantageous to employ a local formulation for the discretized volume fraction gradient  $\nabla f$ , *solely taking into account direct cell face neighbors* [52], which only takes values from

row ( $j$ ) as well. For cell face  $(i + 1/2, j)$  this practice leads to

$$\nabla f_{x_{i+1/2,j}} = \frac{f_{i+1,j} - f_{i,j}}{\Delta x}. \quad (21)$$

The underlying situation for the approximative evaluation of  $\nabla f$  is depicted schematically in Fig. 5 for the 2D case.

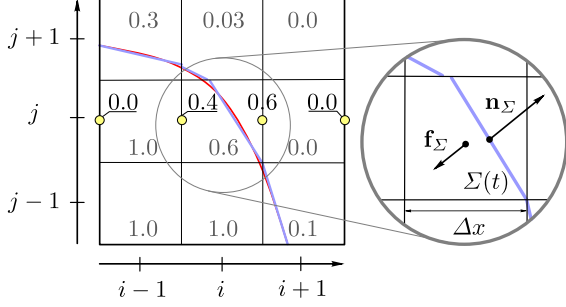


**Figure 5:** Numerical approximation of  $\nabla f$  for row ( $j$ ) based on a narrow stencil (using direct neighbors only) as utilized in this study for force-balanced CSF approach.

#### TURBIT-VOF

**Numerical method.** The TURBIT-VOF code solves the locally volume-averaged two-phase Navier-Stokes equation in non-dimensional single field formulation for two incompressible Newtonian fluids on a regular staggered Cartesian mesh by a Finite Volume Method. In each mesh cell containing both phases, the interface is represented by a plane of zero thickness. The interface evolution is described by the volume fraction equation (15). This equation is solved by a volume-of-fluid method which consists of two steps. In the first step, the interface location is geometrically reconstructed by an in-house PLIC algorithm called EPIRA. On a 3D structured orthogonal non-equidistant fixed grid, it reconstructs a planar interface of any orientation exactly (therefore its name which stands for Exact Plane Interface Reconstruction Algorithm). In the second step the fluxes of the liquid over the cell faces are computed by an unsplit advection scheme. Time integration of the momentum equation is performed by an explicit third order Runge-Kutta method. For approximation of spatial derivatives second order central difference schemes are used. A divergence free velocity field is ensured at the end of each time step by a projection method similar to that in FS3D. The Poisson equation (17) is solved by a conjugate gradient technique. For details we refer to [42, 43, 53].

**Surface tension calculation.** In the volume-averaged single phase momentum equation, the surface tension term is given by

$$\mathbf{f}_\Sigma = \sigma \kappa a_\Sigma \mathbf{n}_\Sigma. \quad (22)$$

Here,  $\kappa = -\nabla_\Sigma \cdot \mathbf{n}_\Sigma$  is twice the mean interface curvature,  $a_\Sigma$  is the volumetric interfacial area density, and  $\mathbf{n}_\Sigma$  is the unit normal vector to the interface. In the volume-averaged formulation, the Dirac delta function  $\delta_\Sigma$  is thus represented by  $a_\Sigma$ .

TURBIT-VOF employs a staggered grid such that the control volumes for the three components of the Navier-Stokes equation are shifted by half a mesh-width. Solving for the velocity components  $u_{i+1/2,j,k}$ ,  $v_{i,j+1/2,k}$ ,  $w_{i,j,k+1/2}$  requires that the surface tension term in Eq. (22) is evaluated at staggered positions, too. We illustrate the procedure for the first component of the Navier-Stokes equation which requires specification of  $a_\Sigma$ ,  $\mathbf{n}_\Sigma$  and  $\kappa$  at position  $(i + 1/2, j, k)$ . These quantities are determined from the known interface position and cell-centered unit normal vector  $\mathbf{n}_{\Sigma;i,j,k}$  (provided by the EPIRA algorithm). We use the following approximations where in single-phase mesh cells  $\mathbf{n}_{\Sigma;i,j,k}$  is set to zero.

The staggered unit normal vector is obtained from the interpolation

$$\mathbf{n}_{\Sigma;i+1/2,j,k} = \frac{\mathbf{n}_{\Sigma;i,j,k} + \mathbf{n}_{\Sigma;i+1,j,k}}{|\mathbf{n}_{\Sigma;i,j,k} + \mathbf{n}_{\Sigma;i+1,j,k}|}. \quad (23)$$

The staggered curvature is computed from the gradient of the unit normal vector

$$\kappa_{i+1/2,j,k} = - \left( \frac{n_{x;i+1,j,k} - n_{x;i,j,k}}{\Delta x_i} + \frac{n_{y;i+1/2,j+1/2,k} - n_{y;i+1/2,j-1/2,k}}{\Delta y_j} + \frac{n_{z;i+1/2,j,k+1/2} - n_{z;i+1/2,j,k-1/2}}{\Delta z_k} \right), \quad (24)$$

where the double-staggered unit normal vectors are given by

$$\begin{aligned} \mathbf{n}_{\Sigma;i+1/2,j\pm 1/2,k} &= \frac{\mathbf{n}_{\Sigma;i,j,k} + \mathbf{n}_{\Sigma;i,j\pm 1,k} + \mathbf{n}_{\Sigma;i+1,j,k} + \mathbf{n}_{\Sigma;i+1,j\pm 1,k}}{\|\mathbf{n}_{\Sigma;i,j,k} + \mathbf{n}_{\Sigma;i,j\pm 1,k} + \mathbf{n}_{\Sigma;i+1,j,k} + \mathbf{n}_{\Sigma;i+1,j\pm 1,k}\|} \\ \mathbf{n}_{\Sigma;i+1/2,j,k\pm 1/2} &= \frac{\mathbf{n}_{\Sigma;i,j,k} + \mathbf{n}_{\Sigma;i,j,k\pm 1} + \mathbf{n}_{\Sigma;i+1,j,k} + \mathbf{n}_{\Sigma;i+1,j,k\pm 1}}{\|\mathbf{n}_{\Sigma;i,j,k} + \mathbf{n}_{\Sigma;i,j,k\pm 1} + \mathbf{n}_{\Sigma;i+1,j,k} + \mathbf{n}_{\Sigma;i+1,j,k\pm 1}\|} \end{aligned} \quad (25)$$

and  $\mathbf{n}_\Sigma = (n_x, n_y, n_z)^T$ .

The staggered interfacial area density is given by  $a_{\Sigma;i+1/2,j,k} = A_{\Sigma;i+1/2,j,k}/V_{i+1/2,j,k}$  where  $A_{\Sigma;i+1/2,j,k}$  is the interfacial area within the staggered mesh cell of volume  $V_{i+1/2,j,k}$ . The interfacial area in the staggered mesh cell  $A_{\Sigma;i+1/2,j,k}$  is determined from the reconstructed interface in the two neighbouring centered mesh cells  $(i, j, k)$  and  $(i + 1, j, k)$ . To this end, the area of the reconstructed planar interfaces in the two half-cells  $[x_{i,j,k}, x_{i+1/2,j,k}] \times [y_{i,j-1/2,k}, y_{i,j+1/2,k}] \times [z_{i,j,k-1/2}, z_{i,j,k+1/2}]$  and  $[x_{i+1/2,j,k}, x_{i+1,j,k}] \times [y_{i,j-1/2,k}, y_{i,j+1/2,k}] \times [z_{i,j,k-1/2}, z_{i,j,k+1/2}]$  is computed and both values are summed up to yield  $A_{\Sigma;i+1/2,j,k}$ .

The described surface tension model is non-standard. Potential advantages are the fully localized representation of the surface tension force, i.e. it is nonzero only in mesh cells that actually contain an interface. This is of benefit for film-like interfaces [54]. Furthermore, the method does not involve any mollification of the volume-fraction. Disadvantageous is that the surface tension force and the pressure gradient do not balance on a discrete level and it is unclear how to achieve this. Another weakness is the computation of the interface curvature. Tests for stationary circular interfaces show that the method is of order zero (i.e. the error of the curvature computation does not reduce if the mesh is refined). To obtain an improved estimation of the interface curvature we are currently implementing a high-function based algorithm.

### 3.2.3. Interface Tracking Method – OpenFOAM (*interTrackFoam*)

OpenFOAM – Open Field Operation And Manipulation – is a free and Open Source C++ Class Library for Computational Continuum Mechanics (CCM) and Multiphysics [55–57]. OpenFOAM features efficient linear equation solvers with polyhedral cell support and is massively parallelized. Its Object-Oriented-Programming enables to mimic data types and basic operations of CCM using top-level syntax as close as possible to the conventional mathematical notation for tensors and partial differential equations. Thus, OpenFOAM renders a versatile and flexible platform for numerical studies in current fields of research related to interfacial flows and complex phenomena involved therein.

**Applied models and methods.** In this benchmark study we employ OpenFOAM’s interface tracking method (*interTrackFoam* solver family). The movement of the deforming interfacial boundary is obtained

as a part of the numerical two-phase flow solution. The interface itself is represented by a computational mesh boundary, the motion of which is accomplished by displacement of corresponding mesh boundary faces and control points. For a detailed description the interested reader is referred to [58, 59].

Using OpenFOAM, the original interface tracking methodology of Muzaferija and Perić [24] has been significantly extended by Tuković and Jasak [58] taking into account viscous and surface tension effects at the interface. The overall solution procedure is based on the iterative Pressure Implicit with Splitting of Operators (PISO) algorithm by Issa [60] for pressure-velocity coupling. The solution procedure is of second-order accuracy in space and time – in particular, it is worth noting that the surface tension calculation is of second order accuracy being based on a force-conservative approach; moreover, the Rhie-Chow interpolation practice has been improved (cf. [58] for details). The numerical method of the interface tracking approach in OpenFOAM comprises collocated (pseudo-staggered) Finite Area Method (FAM), a moving mesh extension to its collocated Finite Volume Method (FVM) on arbitrary polyhedral meshes along with automatic mesh motion [55, 58, 59, 61–63]. Since only small deformations are present, Laplacian mesh motion as described by Jasak et al. [55] is adopted in this study.

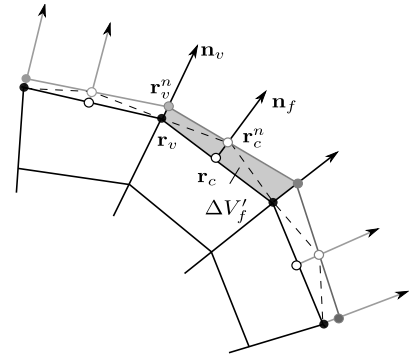


**Figure 6:** Interface Tracking – Interface movement by displacement of corresponding mesh boundary faces and control points.

The algorithm can be described briefly as follows: at the end of each PISO step, which is performed on the mesh being *fixed*, the net mass flux over the interface is non-zero. However, since we do not consider phase change, i.e. no interfacial mass transfer takes place, the net mass flux across the *moving* interface must be zero. Hence, a correction  $\Delta V'_f$  is needed for which the interface points have to be moved (see Fig. 6). For this, con-

control points  $\mathbf{r}_c$  at the center of each boundary face are defined. Next, the displacement directions  $\mathbf{n}_f$  normal to the boundary are computed. In order to determine the mesh displacement magnitude  $h$  at the interface, the discretized Space Conservation Law (SCL) is exploited [64]. Then, the control points are moved along the displacement directions, i.e.

$$\mathbf{r}_c^n = \mathbf{r}_c + h\mathbf{n}_f, \quad (26)$$

and the new positions of vertices  $\mathbf{r}_v^n$  are found applying the least square fit [58].

**Finite Volume and Finite Area Discretization for Dynamic Arbitrary Unstructured Meshes.** We employ the unstructured Finite Volume Method (FVM) for discretization of the governing transport equations within the fluid bulk, while the unstructured Finite Area Method (FAM) is used for discretization of interface conditions and (if required) governing equations on the fluid interface. The discretization procedure is divided into two steps: domain discretization and equation discretization.

*Domain discretization.* Discretization of the computational domain comprises temporal and spatial discretization. The temporal domain is split into discrete time steps  $\Delta t$ , allowing for adaptive time-stepping while solving for the governing equations in a time-marching manner. The bulk flow domains are discretized by decomposing each into a finite number of convex polyhedral control volumes (CVs – or simply cells) of arbitrary shape (unstructured FVM), which do not overlap and completely fill up the spatial domains. Fig. 7a exemplarily depicts a control volume  $V_P$ . Its centroid is denoted  $P$ , while the centroid of a neighboring cell shall be denoted  $N$ . The polygonal cell face separating both cells is denoted  $f$ , where  $\mathbf{S}_f$  is the face area vector normal to the face  $f$  with the magnitude being equal to the face area,  $S_f = \|\mathbf{S}_f\|$ . The spatial discretization of the interfacial domain according to unstructured FAM can be thought of best as a two-dimensional collapse of its FVM counter-part, however, accounting for curvature of the interfacial domain. Fig. 7b shows a polygonal control area  $S_P$ . Its centroid is denoted  $P$ , the neighboring centroid  $N$ . The edge separating both control faces is denoted  $e$  – its length  $L_e$  and corresponding edge unit bi-normal vector  $\mathbf{m}_e$ , which is perpendicular to the edge vector  $\mathbf{e}$  and the edge normal  $\mathbf{n}_e$  and the careful evaluation of which is pivotal for an consistent and accurate surface tension treatment.

*Equation discretization.* A cell-centered (pseudo-staggered) Finite Volume Method for unstructured meshes is applied for discretization of the Navier-Stokes equations. The unstructured Finite Volume/Area discretization is of second-order accuracy, since it is based on the integral form of conservation equations, transforms the surface integrals into sums of face integrals and approximates them along with the volume integrals to second-order accuracy by employing the mid-point rule.

For all dependent variables we use central differencing, that is we employ linear interpolation to calculate the face-centered values from neighboring cell-centered values. A notable exception is the convective term within the linear momentum equation, where we employ the Gamma discretization scheme with deferred correction [65] – locally blending second-order accurate linear interpolation with the unconditionally bounded upwind interpolation to ensure boundedness and stability. The diffusive term is discretized implicitly using linear interpolation with explicit non-orthogonal correction. Temporal discretization is accomplished by means of the second-order accurate implicit three time level scheme commonly referred to as backward scheme.

**Surface tension calculation.** As for interface capturing methods, inaccuracies or inconsistencies in surface tension calculation will cause unphysical so-called parasitic or spurious currents to arise at the interface. As a consequence, not only accuracy but also stability and robustness of a solution method might become severely biased. Hence OpenFOAM's interface tracking method employs a novel force-conservative procedure for surface tension calculation.

To include surface tension and viscous effects, the dynamic boundary conditions are evaluated as a Dirichlet pressure boundary condition at the interface. For surface tension treatment, Tuković and Jasak derived the force-conservative approach – details are provided in [58, 59]. The surface divergence is evaluated according to Weatherburn [66]. In what follows, we briefly describe the conceptual approach of the force-conservative surface tension calculation.

Given a fluid interface discretized by arbitrary polygonal control areas (as depicted in Fig. 7b) constituting an unstructured surface mesh which separates two bulk fluid domains, the corresponding surface tension force

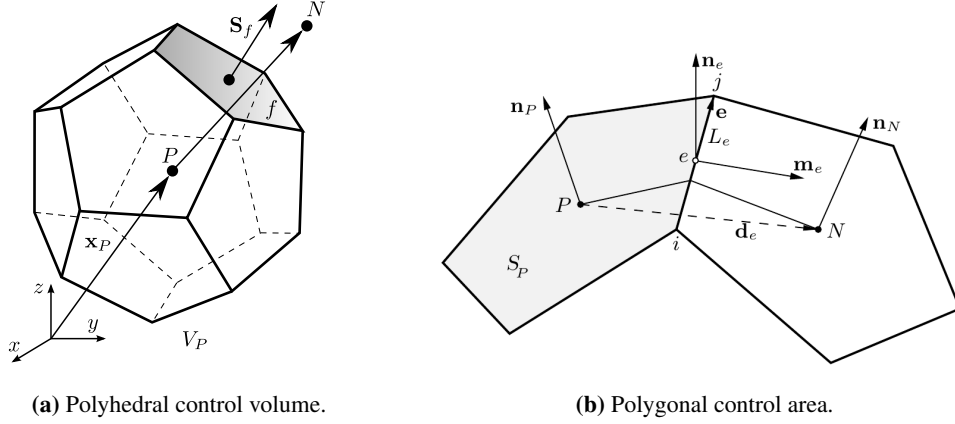


**Figure 7:** Control volume resp. area for unstructured Finite Volume and Finite Area Method.

acting on a single control area  $S_f$  reads:

$$\mathbf{F}_{S_f}^\sigma = \oint_{\partial S_f} \mathbf{m} \sigma dL = \sum_e \int_{L_e} \mathbf{m} \sigma dL = \sum_e (\sigma \mathbf{m})_e L_e. \quad (27)$$

With  $L_e$  denoting the edge lengths,  $(\sigma \mathbf{m})_e$  is to be interpreted as the surface tension force per unit length. Obviously, such an approach ensures the surface tension force  $\mathbf{F}_{S_f}^\sigma$  of the closed polygonal surface  $S_f$  becoming exactly zero, if  $(\sigma \mathbf{m})_e$  is evaluated accurately and  $(\sigma \mathbf{m})_e$  for two control areas are parallel but opposite in sign taking the same value in magnitude.

Applying the surface divergence theorem and the midpoint rule and further assuming a constant surface tension coefficient,  $\mathbf{F}_{S_f}^\sigma$  can be rewritten as (cp. Fig. 7b)

$$\mathbf{F}_{S_f}^\sigma = \int_{S_f} \sigma \kappa \mathbf{n} dS \approx \sigma \kappa_f \mathbf{n}_f S_P. \quad (28)$$

However, equivalently we use

$$\mathbf{F}_{S_f}^\sigma = \sigma (\mathbf{n}_i \mathbf{n}_j) \cdot \sum_e \mathbf{m}_e L_e, \quad (29)$$

where the last identity merely states the fact that the normal component of the surface tension force  $\mathbf{F}_{S_f}^\sigma$  according to Eqn. (27) equals  $\int_{S_f} \sigma \kappa \mathbf{n} dS$  representing the normal contribution to  $\mathbf{F}_{S_f}^\sigma$ .

The inherent fulfillment of the total surface tension force becoming exactly zero on a closed surface is achieved within the numerical method by ensuring a

- i) consistent evaluation of *both* the normal *and* tangential components of  $\mathbf{F}_{S_f}^\sigma$  (even for constant surface tension coefficients as presumed in this study),
- ii) accurate approximation of the surface tension force per unit length  $(\sigma \mathbf{m})_e$ .

Both aspects render pivotal for a force-conservative approach to surface tension calculation within an interface tracking framework:

ad i) On an unstructured polygonal surface mesh the normal of a face area  $S_f$  is commonly determined by triangulation (face decomposition into triangles) and adequate averaging of the normals of resulting triangles. Consequently, in order to ensure force-conservativeness, the tangential part of the surface tension force has to be taken into account as well (even for cases with constant surface tension coefficient). The implementation is done analogous to Eqn. (29).

ad ii) The relevant bi-normal unit vector  $\mathbf{m}_e$  in the surface tension force per unit length term is calculated as

$$(\sigma \mathbf{m})_e = \sigma \frac{\mathbf{e}}{\|\mathbf{e}\|} \times \frac{\mathbf{n}_i + \mathbf{n}_j}{2}, \quad (30)$$

where  $\mathbf{n}_i$  and  $\mathbf{n}_j$  denote the interfacial unit normal vectors in face points  $i$  and  $j$ , respectively (cp. Fig. 7b). Note that a constant surface tension coefficient has been assumed in which case  $\sigma_i = \sigma_j = \sigma$ . In doing so, the accuracy of the approximation of  $(\sigma \mathbf{m})_e$  inherently depends on the accuracy of the approximation of interfacial normal vectors in control area vertices. These are calculated by means of

least squares bi-quadratic surface fittings using the respective local coordinate systems (cf. [58] for details). Alternatives such as a pairwise-weighted averaging of normal vectors from neighboring edges adjacent to a vertex has proven less accurate and, hence, shall be disregarded in this study.

#### 4. Results and Discussion

We consider the quasi-stationary case of an upward rising Taylor Bubble which is moving due to buoyancy and pressure forces in an infinitely long square channel with cross section  $1.98 \text{ mm} \times 1.98 \text{ mm}$ . The fluid system considered consists of glycerin and water constituting the liquid phase and air as the gaseous phase (cf. section 2 for details on the experimental setup). The bubble volume is  $17.5 \text{ mm}^3$ . The material properties of the liquid are given by the density  $\rho_L = 1195.6 \text{ kg/m}^3$  and viscosity  $\eta_L = 28.54 \cdot 10^{-3} \text{ kg/ms}$ ; those of the gas phase are given by the density  $\rho_G = 1.3 \text{ kg/m}^3$  and viscosity  $\eta_G = 20 \cdot 10^{-6} \text{ kg/ms}$ . The surface tension coefficient is  $\sigma = 66.69 \cdot 10^{-3} \text{ kg/s}^2$ . The stationary rising velocity of the Taylor bubble has been determined as  $v_b = 205.57 \text{ mm/s}$  with a co-current underlying flow.

##### 4.1. Case setup & Solution control

**Case setup.** In order to set up the case of an infinitely long square channel with a single rising Taylor bubble in co-current flow, different method- and code-specific approaches have been chosen – namely a periodic unit cell approach (DROPS and TURBIT-VOF), a moving window technique (FS3D) and a Moving Reference Frame (MRF) technique (OpenFOAM – `channelBubbleInterTrackFoam`). The different approaches and set boundary conditions are depicted in Fig. 8.

*Periodic unit cell approach.* We consider a periodic unit cell of length  $6d_h$ , where  $d_h = 1.98 \text{ mm}$  is the hydraulic diameter. Periodicity is applied for the bottom and top face of the simulation domain (cp. Fig. 8a), whereas standard no-slip boundary conditions hold for all other boundaries. In order to render the periodicity condition physically meaningful we subtract the a given linear decreasing part from  $p$  obtaining  $\tilde{p}$ , which is the periodic part of the pressure and serves as an unknown field in the simulations. The linear decreasing part acts as a driving force to the system, being adjusted s.t. the desired target value for the bubble velocity is achieved up to a certain tolerance.

Moreover, the bubble length has been assumed to be considerably smaller than the unit cell length and furthermore the interaction between two periodic bubbles is assumed to be negligible. This assumption seems to be valid as simulations with a unit cell length of  $10d_h$  give comparable results.

*Moving window technique.* The mesh is attached to a moving window, which means that the computational domain is shifted with the Taylor bubble to keep its center of mass in the center of the computational domain. In doing so, it becomes necessary to copy all fields accordingly. Consequently, a new row of computational cells needs to be inserted at the domain's top boundary, with new field values derived from the corresponding boundary conditions (cf. Fig. 8b).

*Moving Reference Frame technique.* A non-inertial frame of reference is attached to the centroid of the rising Taylor bubble. The position of the computational domain is adjusted s.t. the Taylor bubble always remains centered (Moving Reference Frame, MRF); bubble acceleration is considered by means of non-inertial reference frame adjustment due to virtual forces. The effect of rising (resp. frame) velocity and co-current flow velocity is taken into account within the MRF framework (cf. Fig. 8c).

As for initialization, it is worth noting that for the interface tracking case the initial bubble shape has been obtained by spatial discretization of the fluid and Taylor bubble domain, each separately – enforcing a conformal interfacial patch. We employed the mesh module of Salome v. 6.4.0 (Netgen algorithms). In order to ensure an initial shape which is close to the stationary solution of the Taylor bubble and moreover exhibits the reference volume, we made use of a semi-analytical axisymmetric solution provided by Wörner et al. [67] based on work of Dumitrescu [9] for a Taylor bubble rising in a vertical tube under the assumption of potential flow.

The simulation in the Finite Element code DROPS used meshes which have been adaptively refined two times towards the interface, resulting in approximately 321,000 velocity unknowns and 26,000 pressure unknowns, where the number of unknowns is not constant due to adaptive refinement/coarsening steps within the simulation. Where the film thickness is smallest, the film is only resolved by two velocity unknowns. However, note that the approximation of the velocity field is piecewise quadratic. As for the Finite Volume codes, the numerical simulation with FS3D have been accom-

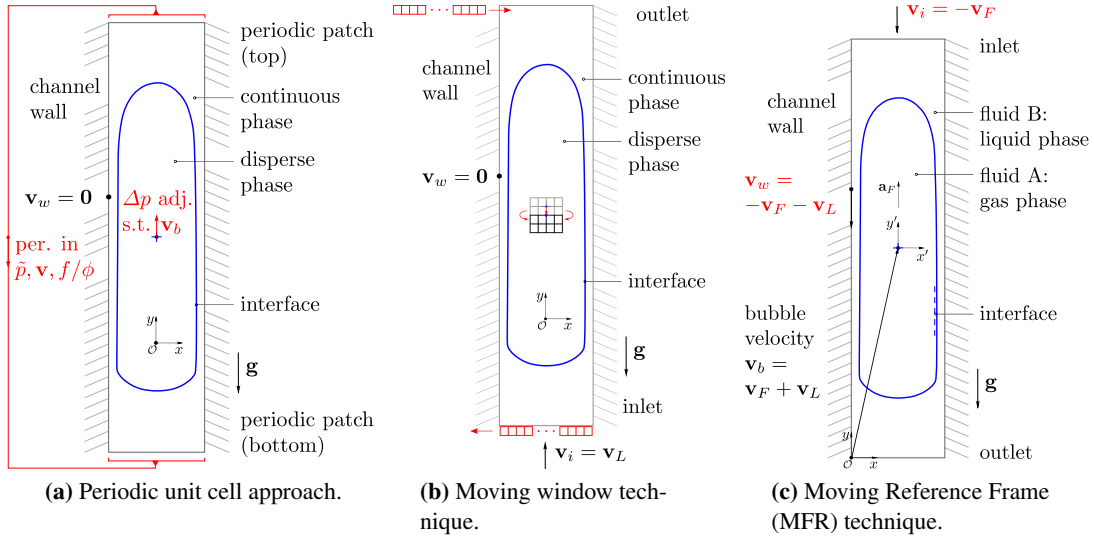


**Figure 8:** Different approaches to case setup of Taylor bubble flow in a channel.

plished using a uniform mesh density of 512 cells in vertical and 64 cells in both horizontal directions, where symmetry boundary conditions were used in order to reduce the overall size of the computational domain while maintaining a sufficient mesh resolution. The computations in TURBIT-VOF have been performed without any assumption regarding symmetry. The mesh is uniform as well with 80 mesh cells in both horizontal directions and 480 mesh cells in the vertical direction. For OpenFOAM interface tracking simulations the mesh comprised of 156,208 polyhedra and 200 hexahedra with a spatial resolution adaptively increasing towards the interfacial boundary. Thereby, the spatial resolutions for the Finite Volume codes correspond to a resolution of the liquid film in the lateral cut by at least 2-3 mesh cells.

**Solution control.** Since we consider a quasi-stationary case, a stop-criterion for simulation runs is central and needs to be carefully defined for all codes employed in this study: we found the bubble terminal rising velocity along with the bubble length to be sensitive criteria to assess quasi-stationarity of the flow state. If both are converged up to a prescribed tolerance, the numerical solution is considered quasi-stationary and consequently the simulation is stopped.

#### 4.2. Simulation Results

Results are presented in Tab. 1 and in Figs. 9 and 10. For a quantitative comparison of the shape of Taylor bubble by means of geometrical target quantities,

we consider the bubble length and the film thickness at locations, where deficiencies in surface tension calculation procedures become visible. Moreover, the cuts through the bubble surface yield shape profiles which enable for a local analysis and discussion of deviations from the experimentally obtained bubble shape.

**Target quantities.** Geometrical target quantities for a quantitative validation are depicted in Tab. 1 along with the corresponding deviations from the experimental reference value. Moreover, we provide uncertainties for the experimental reference values.

For the evaluation of minimal film widths within the lateral and diagonal cutting plane, we calculate the distances of the bubble surface to the channel axis at distinct axial positions. Then, the two maximum values in distance within the lateral and diagonal cutting planes, respectively, correspond to minimal values in film thickness in these planes. Note in passing that – specific to the underlying approach – we either used iso-surfaces (interface capturing) or the interfacial surface mesh (interface tracking) for approximating the position of the bubble surface from discrete data. The length of the Taylor bubble is calculated from the maximum and minimum of the longitudinal component of interface position vector, which again can be obtained from the approach-specific interface representation.

**Shape profiles.** Shape profiles of the Taylor bubble are gained from diagonal and lateral cutting planes by



intersection with the respective interfacial surface representation (iso-surface or surface mesh) – cf. Fig. 9. A corresponding close-up view is shown exemplarily for the lateral cutting plane in Fig. 10.

The terminal bubble velocity has been evaluated as 206.92 mm/s ( $\Delta p = 267.4$  Pa), 205.43 mm/s, 207.8 mm/s ( $\Delta p = 275.57$  Pa) and 205.67 mm/s for DROPS, FS3D, TURBIT-VOF and OpenFOAM (channelBubbleInterTrackFoam), respectively. Experimentally the terminal rising velocity of the Taylor bubble has been determined to  $v_b = 205.57 \pm 0.82$  mm/s. Note that the corresponding pressure differences have been provided in brackets for approaches where the pressure difference for the given bubble velocity has been adjusted.

#### 4.3. Discussion

A quantitative validation for the given case of a single rising Taylor bubble in a square milli-channel is achieved by both examining the bubble’s shape profiles in lateral and diagonal cuts through the flow domain, and by comparing with geometrical target quantities related to the bubble shape. The obtained validation quantities are provided in Tab. 1. The bubble’s shape profile is depicted in Fig. 9 and 10.

While for comparability of the bubble tip and rear profiles, the shapes have been vertically aligned to each other in Fig. 10 (both in 10a and 10b), this is intentionally not done in Fig. 9, where the shape profiles have been aligned to a common position of the bubble tips. From comparing solely the bubble shapes provided in Fig. 10 one might conclude, that all solvers show very similar results. In particular, the interfacial curvatures are well captured for the bubbles’ tip part, and still a decent agreement with the experimental reference could be declared for its rear part. However, examining the bubble shapes as shown in Fig. 9 (cp. the error bar in Inset A of Figs. 9a and 9b), a closer study of uncertainties and possible error sources is advisable before judging the agreement between numerical and experimental results. Distinct experimental uncertainties which give rise to errors and consequently constitute possible reasons for deviations between experimental and numerical results are to be discussed.

Main contributions to uncertainty in our numerical results (beside numerical errors) stem from three sources of experimental uncertainties – entering the resulting quality of our numerical simulations both directly and indirectly. The experimentally determined bubble volume is subject to uncertainty and an inaccurate initial

bubble volume would directly result in erroneous numerical results, in particular a wrong length of the Taylor bubble. Moreover, prescribing an inaccurate rising velocity would directly impact both the solution control (stop criterion for quasi-stationarity) and possibly the numerical setting itself in terms of the boundary conditions imposing a wrong pressure gradient over the channels height (cp. periodic unit cell approach depicted in Fig. 8a). Indirectly, an inaccurate length of the Taylor bubble could lead to wrong conclusions whether the agreement between experimental and numerical results can be declared acceptable.

As for the first aspect of a correct initial bubble volume, the numerical initialization procedures themselves need to be assessed with respect to their accuracy as well. However, inaccuracies due to initialization has been found negligible. The precision of initialization procedures with respect to the reference bubble volume reached from utmost accurate (machine tolerance for the LS method) to a small relative error of about  $2 \cdot 10^{-1}\%$  due to the meshing procedure for initialization of the interface tracking simulations. The initial volume error for the VOF methods has been found to be  $3 \cdot 10^{-3}\%$  (at maximum) due to geometrical tolerances during PLIC interface construction. The tolerable error between experimental and simulation results is 0.8% for the bubble length and 0.1% for the film thickness. Note that the measurement error bound for the bubble lengths has been estimated as 0.41%. The experimentally determined bubble volume, which is used to initialize the numerical simulations, has an error of 0.39%. Thus, this leads to another (indirect) contribution to the measurement-induced error of the simulated bubble length of the same magnitude, such that the overall error bound used for the assessment of numerical results is 0.8%.

Concluding, we find in view of the discussion in section 2 regarding the accuracy of the measurements and initialization procedures, and from the error bar depicted in Figs. 9a and 9b that all solvers (though they employ very different state-of-the art approaches to surface tension calculation) do show similar results, and a good agreement between numerical and experimental results can be declared. Moreover, the geometrical target quantities for validation as provided in Tab. 1, i.e. the obtained lengths of the Taylor bubble and the minimal film thicknesses in lateral and diagonal cuts, do show acceptable agreement both between numerical and experimental results as well as among the numerical simulation results.

Note in passing that the topic of numerical accuracy, efficiency and stability is not within the scope of

**Table 1:** Validation results – Geometrical target quantities and deviations from experimental mean reference values.

	DROPS	FS3D	TURBIT-VOF	OpenFOAM*	Experiment
bubble length	7.23 mm (0.42%)	7.201 mm (0.01%)	7.12 mm (1.12%)	7.16 mm (0.56%)	7.20±0.06 mm
min. film thickness (diagonal cut)	0.4392 mm (1.41%)	0.4344 mm (3.00%)	0.4331 mm (0.00%)	0.4305 mm (0.45%)	0.4331±0.0004 mm
min. film thickness (lateral cut)	0.049 mm (3.06%)	0.049 mm (3.06%)	0.051 mm (2.00%)	0.047 mm (7.44%)	0.0505±0.0001 mm

(\*) Solver `channelBubbleInterTrackFoam`: modified version of `bubbleInterTrackFoam` as publicly released in OpenFOAM-ext v. 1.6.

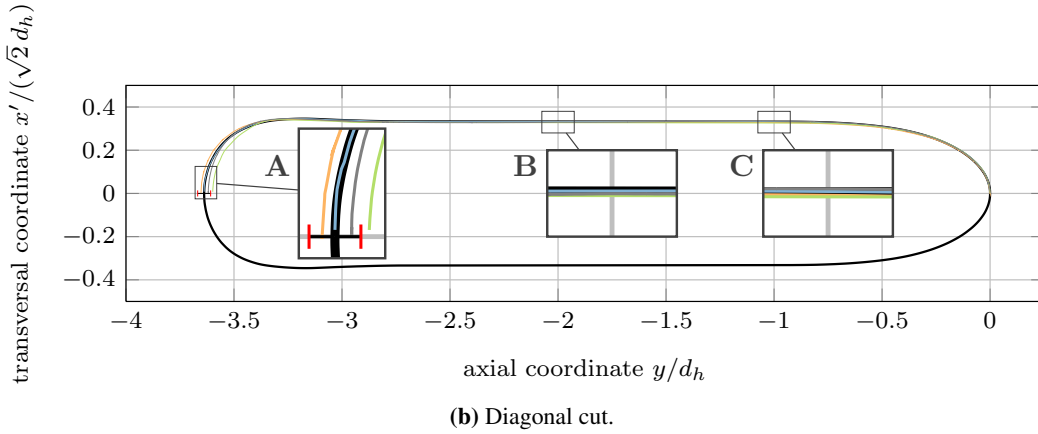
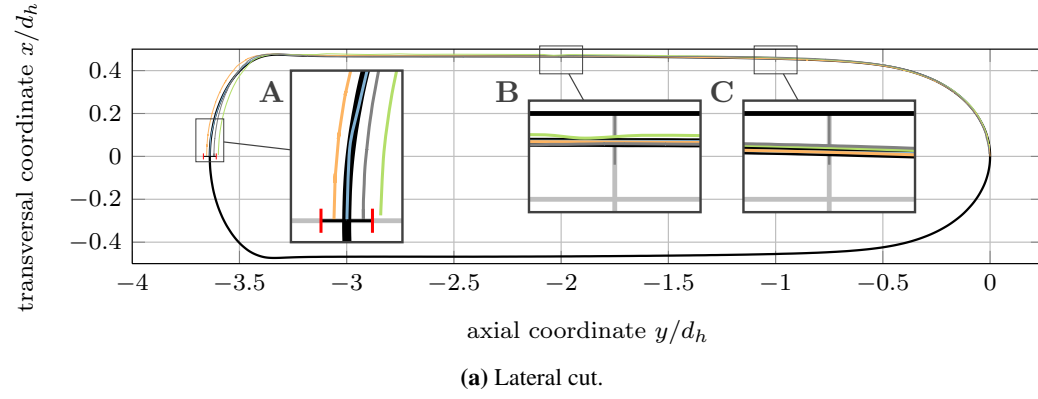


**Figure 9:** Shape profile of Taylor bubble for distinct cutting planes through flow domain.

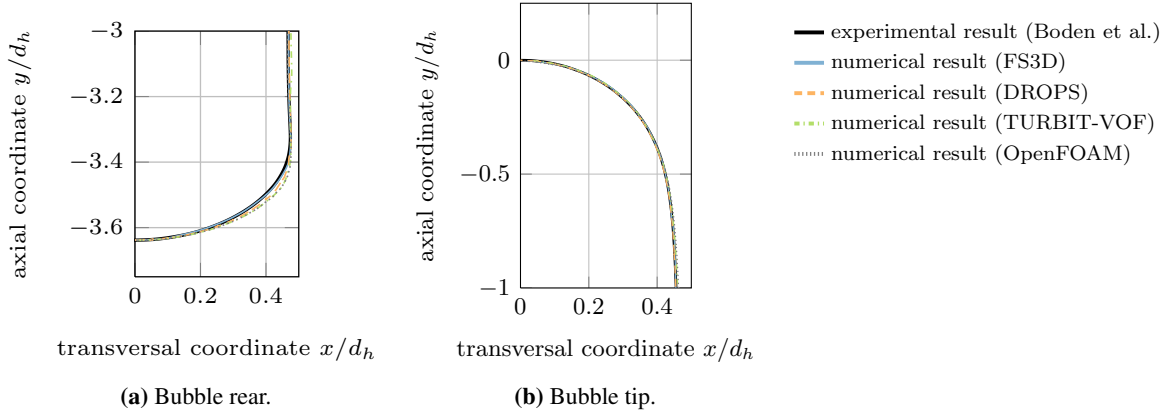


**Figure 10:** Close-up view of Taylor bubble tip and rear for lateral cutting plane.

the present study and will be addressed in future work. However, it is the authors' intention to pass over some experiences and observations to the reader which are related to the above aspects and were gained in this study employing the particular interfacial solvers.

- For a meaningful validation, the use of sensitive and (wherever possible) local and three-dimensional data is highly recommended.

The use of a mean film width, for instance, which is averaged over a reference length (e.g. the hydraulic channel diameter), is rather insensitive w.r.t. to different numerical approaches and discretization practices, and thus does not reveal possible deficiencies as can be seen from Fig. 9a, where the mean film thickness in all cases would still indicate good agreement. As a better target quantity for validation, it should be replaced by the length of the Taylor bubble, which is much more sensitive and more accessible in experiments. Additionally, the evaluation of minimal film thickness is recommended, since their value has been found to be subject of notable changes during the simulations – at a location, where any change of the numerical method for surface tension calculation has significant influence w.r.t. the interface location. Moreover, the evaluation of the minimal film thickness in both the lateral and diagonal cutting plane captures the influence of the  $Ca$  number on the bubble shape, since the Taylor bubble penetrates into the corners of the square channel for low values of  $Ca$  (cp. Tab. 1).

- For a high-fidelity surface-tension treatment one has to consider both accurate and consistent numerical approximation of interfacial force densi-

ties (interface capturing methods) and interfacial force per unit length vectors (interface tracking methods). Balanced-force and – where this is inherently ensured (e.g. for the discretization practice underlying the interface tracking methodology) – force-conservative approaches to surface tension calculation are central.

For interface tracking methods, the use of least squares bi-quadratic surface fitting for the approximation of interfacial normal vectors in control area vertices seems advisable for an accurate surface tension calculation. When applying level-set techniques to a 'sharp-interface' surface tension treatment the question for an approximate interface with discrete normals which allow to apply numerical integration arises. The level-set function is an approximation to a signed distance function. Exploiting this property for the derivation of interfacial normals is crucial in order to render the surface tension discretization accurate. In the context of finite element approximations for the momentum equation it is important to provide pressure approximations with discontinuities at the discrete interface in order to compensate for the locality of the surface tension force. For Volume-of-Fluid methods, the accuracy and consistent choice of a (narrow) computational stencil for discretization of the interfacial normal approximation renders crucial. In particular, as a recent study with TURBIT-VOF has shown for a 2D test case with circular interface, a height-function based approach to curvature calculation is of a higher accuracy and better convergence than the method currently implemented. However, the method needs to be extended to 3D, and thus a comparison with the pre-

sented 3D benchmark problem of a single rising Taylor bubble shall be subject to future publications.

## 5. Summary & Conclusions

The present study is devoted to validation of interfacial two-phase flow solvers, examining the shape of a single rising Taylor bubble in a square milli-channel. By means of a quantitative comparison of simulation results from conceptually different interface capturing and tracking methods with a detailed and local experimental data basis, we propose this benchmark experiment to form a basis for other methods and codes. In particular, the presented Taylor bubble benchmark with its emphasis on an exact evaluation of the bubble's shape and geometrical target quantities is considered to provide a reasonable basis for the assessment of applicability and validity of different method-inherent approaches to surface tension calculation both for interface capturing and tracking techniques.

## Acknowledgement

The authors wish to thank the German Research Foundation (DFG) for financial support within the Priority Program SPP 1506 "Transport Processes at Fluidic Interfaces" with the projects BO 1879/9-1, RE 1461/2-1, WO 1682/1-1 and HA 3088/7-1.

The first author (H.M.) thanks Dr. Željko Tuković (FSB, Univ. Zagreb) for valuable comments and for a bug fix kindly provided. The authors further kindly acknowledge the provision of beamtime by the synchrotron radiation source ANKA, and we acknowledge the kind support by T. Rolo during the operation of the TOPO/TOMO beamline, which is directed by Prof. T. Baumbach, KIT.

## References

- [1] Angeli P, Gavrilidis A. Hydrodynamics of Taylor flow in small channels: A review. *P I Mech Eng C-J Mec* 2008;222(5):737–51.
- [2] Gupta R, Fletcher D, Haynes B. Taylor flow in microchannels: A review of experimental and computational work. *J Comput Multiphase Flows* 2010;2(1):1–32.
- [3] Aussilous P, Quere D. Quick deposition of a fluid on the wall of a tube. *Phys Fluids* 2000;12:2367.
- [4] Kreutzer MT, Kapteijn F, Moulijn J. A., Heiszwolf JJ. Multiphase monolith reactors: chemical reaction engineering of segmented flow in microchannels. *Chem Eng Sci* 2005;60(22):5895–916.
- [5] Thulasidas TC, Abraham MA, Cerro RL. Bubble-train flow in capillaries of circular and square cross section. *Chem Eng Sci* 1995;50(2):183–99.
- [6] Kolb WB, Cerro RL. Coating the inside of a capillary of square cross section. *Chem Eng Sci* 1991;46:2181–95.
- [7] Keskin O, Wörner M, Soyhan H, Bauer T, Deutschmann O, Lange R. Viscous co-current downward Taylor flow in a square mini-channel. *AIChE J* 2010;56(7):1693–702.
- [8] Hysing S, Turek S, Kuzmin D, Parolini N, Ganesan E, Tobiska L. Quantitative benchmark computations of two-dimensional bubble dynamics. *Int Journal Numer Methods Fluids* 2008;60:1259–88.
- [9] Dumitrescu DT. Strömung an einer luftblase im senkrechten rohr. *Zeitschrift für Angewandte Mathematik und Mechanik* 1943;23(3):139–49.
- [10] Davies RM, Taylor GI. The mechanics of large bubbles rising through extended liquids and through liquids in tubes. *Proceedings of the Royal Society of London, Series A: Mathematical, Physical and Engineering Sciences* 1950;200(1062):375–90.
- [11] Irandoust S, Andersson B. Liquid film in Taylor flow through a capillary. *I&EC research* 1989;28(11):1684–8.
- [12] Haase S, Bauer T. New method for simultaneous measurement of hydrodynamics and reaction rates in a mini-channel with Taylor flow. *Chem Eng J* 2011;176-177:65–74.
- [13] Rack A, Weitkamp T, Trabelsi SB, Modregger P, Cecilia A, dos Santos Rolo T, et al. The micro-imaging station of the topotomo beamline at the anka synchrotron light source. *Nuclear Instruments and Methods in Physics Research Section B: Beam Interactions with Materials and Atoms* 2009;267(11):1978–88.
- [14] Gallant RW. Physical properties of hydrocarbons. 14. propylene glycols and glycerine. *Hydrocarbon Processing* 1967;46(5):201–15.
- [15] Unverdi SO, Tryggvason G. A Front-Tracking method for viscous, incompressible, multi-fluid flows. *J Comput Phys* 1992;100:25–37.
- [16] Osher S, Sethian JA. Fronts propagating with curvature-dependent speed: Algorithms based on Hamilton-Jacobi formulations. *J Comput Phys* 1988;79:12–49.
- [17] Sethian JA. *Level Set Methods: Evolving interfaces in geometry, Fluid mechanics, computer vision, and material science*. Cambridge Univ. Press; 1996.
- [18] Sethian J. *Level Set Methods and Fast Marching Methods: Evolving Interfaces in Computational Geometry, Fluid Mechanics, Computer Vision, and Materials Science*. Cambridge University Press; 1999.
- [19] Osher S, Fedkiw J, Ronald P. *Level Set Methods and Dynamic Implicit Surfaces*. Springer; 2002.
- [20] DeBar R. Fundamentals of the KRAKEN code. [Eulerian hydrodynamics code for compressible nonviscous flow of several fluids in two-dimensional (axially symmetric) region]. *Tech. Rep.*; California Univ., Livermore (USA). Lawrence Livermore Lab.; 1974.
- [21] Noh W, Woodward P. *Lecture Notes in Physics*; vol. 59; chap. SLIC (simple line interface calculation). Berlin/New York: Springer; 1976, p. 330–40.
- [22] Hirt C, Nichols B. Volume of fluid (VOF) method for the dynamics of free boundaries. *J Comput Phys* 1981;39(1):201–25.
- [23] Demirdžić I, Perić M. Finite Volume Method for prediction of fluid flow in arbitrarily shaped domains with moving boundaries. *Int J Numer Meth Fluids* 1990;10:771–90.
- [24] Muzaferija S, Perić M. Computation of free-surface flows using the Finite Volume Method and moving grids. *Num Heat Transfer* 1997;Part B 32:369–84.
- [25] Groß S, Peters J, Reichelt V, Reusken A. The DROPS package for numerical simulations of incompressible flows using parallel adaptive multigrid techniques. Preprint 227; IGPM, RWTH Aachen; 2002.
- [26] Groß S, Reusken A. Finite element discretization error analysis

- of a surface tension force in two-phase incompressible flows. *SIAM J Numer Anal* 2007;45:1679–700.
- [27] Groß S, Reusken A. *Numerical Methods for Two-phase Incompressible Flows*. Berlin: Springer; 2011.
- [28] DROPS. The DROPS package. <http://www.igpm.rwth-aachen.de/DROPS/>; Jan. 2013.
- [29] Chang YC, Hou TY, Merriman B, Osher S. A level set formulation of Eulerian interface capturing methods for incompressible fluid flows. *J Comp Phys* 1996;124:449–64.
- [30] Pillapakkam SB, Singh P. A level-set method for computing solutions to viscoelastic two-phase flow. *J Comput Phys* 2001;174:552–78.
- [31] Sussman M, Almgren AS, Bell JB, Colella P, Howell LH, Welcome ML. An adaptive level set approach for incompressible two-phase flows. *J Comput Phys* 1999;148:81–124.
- [32] Tornberg AK, Engquist B. A finite element based level-set method for multiphase flow applications. *Comp Vis Sci* 2000;3:93–101.
- [33] Groß S, Reusken A. Parallel multilevel tetrahedral grid refinement. *SIAM J Sci Comput* 2005;26(4):1261–88.
- [34] Groß S, Reusken A. An extended pressure finite element space for two-phase incompressible flows. *J Comp Phys* 2007;224:40–58.
- [35] Roos HG, Stynes M, Tobiska L. *Numerical Methods for Singularly Perturbed Differential Equations — Convection-Diffusion and Flow Problems*; vol. 24 of *Springer Series in Computational Mathematics*. second ed.; Berlin: Springer-Verlag; 2008.
- [36] Rieber M. *Numerische Modellierung der Dynamik freier Grenzflächen in Zweiphasenströmungen*. Fortschrittberichte VDI / 7; VDI-Verl.; 2003. ISBN 9783183459070.
- [37] Bothe D, Kröger M, Warnecke HJ. A VOF-based conservative method for the simulation of reactive mass transfer at deformable bubbles. *Fluid Dynamics & Materials Processing* 2011;7(3):303–16.
- [38] Bothe D, Fleckenstein S. Modeling and VOF-based numerical simulation of mass transfer processes at fluidic particles; 2013. Revised version under review for *Chem. Eng. Sci.*
- [39] Focke C, Bothe D. Direct numerical simulation of binary off-center collisions of shear thinning droplets at high Weber numbers. *Phys Fluids* 2012;24(7):073105 (pages 18).
- [40] Gotaas C, Pavel H, Jakobsen H, Svendsen H, Hase M, Roth N, et al. Effect of viscosity on droplet-droplet collision outcome: Experimental study and numerical comparison. *Phys Fluids* 2007;19:102106.
- [41] Albert C, Raach H, Bothe D. Influence of surface tension models on the hydrodynamics of wavy laminar falling films in Volume of Fluid-simulations. *International Journal of Multiphase Flow* 2012;43(43):66–71.
- [42] Sabisch W. *Dreidimensionale numerische Simulation der Dynamik von aufsteigenden Einzelblasen und Blasenschwärmen mit einer Volume-of-Fluid Methode*. Ph.D. thesis; University Karlsruhe; 2000.
- [43] Ghidersa B, Wörner M, Cacuci D. Exploring the flow of immiscible fluids in a square mini-channel by direct numerical simulation. *Chem Eng J* 2004;101:285.
- [44] Giusti E. *Minimal Surfaces and Functions of Bounded Variation*. No. 80 in *Monographs in Mathematics*; Boston u.a.: Birkhäuser; 1984. ISBN 3764331534.
- [45] Rider WJ, Kothe DB. Reconstructing volume tracking. *J Comput Phys* 1998;141(2):112–52.
- [46] Chorin A. Numerical solution of the Navier-Stokes Equations. *Math Comput* 1968;22(104):745–62.
- [47] Lafaurie B, Nardone C, Scardovelli R, Zaleski S, Zanetti G. Modelling merging and fragmentation in multiphase flows with surfer. *J Comp Phys* 1994;113:134–147.
- [48] Brackbill J, Kothe D, Zemach C. A continuum method for modeling surface tension. *J Comput Phys* 1992;100(2):335–54.
- [49] Francois MM, Cummins SJ, Dendy ED, Kothe DB, Sicilian JM, Williams MW. A balanced-force algorithm for continuous and sharp interfacial surface tension models within a volume tracking framework. *J Comput Phys* 2006;213(1):141–73.
- [50] Renardy Y, Renardy M. PROST: a parabolic reconstruction of surface tension for the volume-of-fluid method. *J Comput Phys* 2002;183:400–21.
- [51] Popinet S. An accurate adaptive solver for surface-tension-driven interfacial flows. *J Comput Phys* 2009;228:5838–66.
- [52] Boger M, Schlottke J, Munz C, Weigand B. Reduction of parasitic currents in the DNS VOF code FS3D. In: *12th Workshop on Two-Phase Flow Predictions*. Halle (Saale); 2010.
- [53] Öztas M, Wörner M, Soyhan H. Numerical investigation of the stability of bubble train flow in a square minichannel. *Phys Fluids* 2009;21:042108–1.
- [54] Shepel SV, Smith BL. On surface tension modelling using the level set method. *International Journal for Numerical Methods in Fluids* 2009;59(2):147–71.
- [55] Jasak H, Jemcov A, Tuković Ž. OpenFOAM: A C++ library for complex physics simulations. In: *International Workshop on Coupled Methods in Numerical Dynamics IUC*. Dubrovnik, Croatia; 2007.
- [56] Weller HG, Tabor G, Jasak H, Fureby C. A tensorial approach to computational continuum mechanics using object orientated techniques. *Comput Phys* 1998;12(6):620–31.
- [57] OpenFOAM. The OpenFOAM CFD toolbox. <http://www.openfoam.org>; Jan. 2013.
- [58] Ž. Tuković, Jasak H. A moving mesh finite volume interface tracking method for surface tension dominated interfacial fluid flow. *Comput Fluids* 2012;55(0):70–84.
- [59] Tuković Ž., Jasak H. Simulation of free-rising bubble with soluble surfactant using moving mesh finite volume/area method. In: *6th Int. Conf. on CFD in Oil & Gas, Metallurgical and Process Industries. SINTEF/NTNU, Trondheim, Norway*; 2008.
- [60] Issa RI. Solution of the implicitly discretised fluid flow equations by operator-splitting. *J Comput Phys* 1986;62:40–65.
- [61] Jasak H, Ž. Tuković. Automatic mesh motion for the unstructured finite volume method. *Transaction of FAMENA* 2006;30:1–20.
- [62] Jasak H. Dynamic mesh handling in OpenFOAM. In: *48th AIAA Aerospace Sciences Meeting*. Orlando, Florida; 2009.
- [63] Menon S. A Numerical Study of Droplet Formation and Behavior using Interface Tracking Methods. Ph.D. thesis; University of Massachusetts Amherst; 2011.
- [64] Demirdžić I, Perić M. Space conservation law in finite volume calculations of fluid flow. *Int J Numer Meth Fluids* 1988;8:1037–50.
- [65] Jasak H, Weller HG, Gosman AD. High resolution NVD differencing scheme for arbitrarily unstructured meshes. *Int J Numer Meth Fluids* 1999;31:431–49.
- [66] Weatherburn CE. *Differential geometry in three dimension*. Cambridge University Press, London; 1972.
- [67] Wörner M, Ghidersa B, Shahab A. Numerical study of bubble train flow in a square vertical mini-channel: Influence of length of the flow unit cell. In: *5<sup>th</sup> International Conference on Multiphase Flow, ICMF'04*. 2004.